A neural network-based method for input parameter optimization of edge transport modeling utilizing experimental diagnostics

Yu Luo, S. Xu, Yunfeng Liang, E. Wang, J. Cai, Y. Feng, Detlev Reiter, A. Knieps, Sebastijan Brezinsek, D. Harting, M. Krychowiak, D. Gradic, Pei Ren, D. Zhang, Y. Gao, G. Fuchert, A. Pandey, M. Jakubowski

nuclear fusion
IAEA

PAPER • OPEN ACCESS

A neural network-based method for input parameter optimization of edge transport modeling utilizing experimental diagnostics

To cite this article: Y. Luo *et al* 2025 *Nucl. Fusion* **65** 096016

OPEN ACCESS
IOP Publishing | International Atomic Energy Agency
Nuclear Fusion
Nucl. Fusion **65** (2025) 096016 (11pp)
https://doi.org/10.1088/1741-4326/adf75f

A neural network-based method for input parameter optimization of edge transport modeling utilizing experimental diagnostics

Y. Luo[1,2], S. Xu[1,*], Y. Liang[1,2,*], E. Wang[1], J. Cai[1], Y. Feng[3], D. Reiter[2], A. Knieps[1], S. Brezinsek[1,2], D. Harting[1], M. Krychowiak[3], D. Gradic[3], P. Ren[1,2], D. Zhang[3], Y. Gao[3], G. Fuchert[3], A. Pandey[3], M. Jakubowski[3] and the W7-X Team[a]

[1] Forschungszentrum Jülich GmbH, Institute of Fusion Energy and Nuclear Waste Management—Plasma Physics, Partner of the Trilateral Euregio Cluster (TEC), 52425 Jülich, Germany
[2] Faculty of Mathematics and Natural Science, Heinrich Heine University Düsseldorf, 40225 Düsseldorf, Germany
[3] Max Planck Institute for Plasma Physics, 17491 Greifswald, Germany

E-mail: s.xu@fz-juelich.de and y.liang@fz-juelich.de

Received 29 April 2025, revised 28 July 2025
Accepted for publication 4 August 2025
Published 14 August 2025

Abstract

A neural network-based method is developed to fast optimize EMC3-EIRENE input parameters, enabling EMC3-EIRENE to produce synthetic data that closely match experimental measurements on Wendelstein 7-X. Initially, an EMC3-EIRENE simulation database covering a range of key input parameters is generated. Trained on this database, a feed-forward neural network (FNN) surrogate model efficiently maps EMC3-EIRENE input parameters to synthetic signals corresponding to experimentally observed physical quantities. Subsequently, the trained surrogate model is incorporated into a Bayesian inference framework with Dynamic Nested Sampling to infer posterior distributions of the EMC3-EIRENE input parameters. In this step, the FNN-predicted synthetic data are compared with the experimental data, and the likelihood function explicitly accounts for the measurement uncertainties of the selected diagnostics. EMC3-EIRENE simulations using the maximum *a posteriori* estimates derived from these posterior distributions reproduce experimental measurements with satisfactory accuracy.

[a] See Grulke *et al* 2024 (https://doi.org/10.1088/1741-4326/ad2f4d) for the W7-X Team.
[*] Authors to whom any correspondence should be addressed.

This neural network-based method significantly reduces computational costs and the need for manual parameter tuning, and it can be generalized to other similar modeling codes.

Keywords: machine learning, Bayesian inference, EMC3-EIRENE, Wendelstein 7-X

(Some figures may appear in colour only in the online journal)

1. Introduction

Edge plasma transport modeling plays a crucial role in understanding edge plasma behavior and optimizing the design of fusion devices. This is particularly important for devices with complex three-dimensional edge structures, such as Wendelstein 7-X (W7-X), where boundary diagnostics are limited to localized regions, complicating transport analysis. The three-dimensional transport code EMC3-EIRENE [1], which integrates the fluid model EMC3 [2] with the kinetic neutral particle transport code EIRENE [3], can effectively handle configurations with complex edge structures, and has been widely applied in both tokamaks and stellarators for interpreting experimental observations and conducting predictive simulations [4–12]. However, since EMC3-EIRENE describes anomalous transport with a diffusion model, free input parameters (the cross-field transport coefficients) are unavoidable and need to be determined by comparison with the experimental data. Achieving alignment between EMC3-EIRENE simulations and diagnostic measurements typically requires repeated manual parameter adjustments, making the process both time-consuming and computationally intensive. To overcome this problem, it is essential to establish a clear relationship between EMC3-EIRENE input parameters and the experimental measurements, and to develop an automated procedure that rapidly determines the code inputs. In this context, a neural network-based surrogate model provides a promising solution.

Recently, machine learning has been widely applied in fusion research, including the plasma control [13–15], disruption predictions [16–18], and simulation accelerations [19–21], owing to its exceptional capabilities in classification, regression, and pattern recognition. In this study, we propose a combined approach that integrates a feed-forward neural network surrogate model with a Bayesian inference framework utilizing Dynamic Nested Sampling [22]. Initially trained on an EMC3-EIRENE simulation database, the feed-forward neural network (FNN) surrogate learns relationships between input parameters and the synthetic signals of selected diagnostics. Bayesian inference is then employed to systematically determine the posterior distributions of EMC3-EIRENE input parameters by quantitatively comparing the surrogate-generated synthetic data with experimental measurements, explicitly incorporating measurement uncertainties. Notably, this process can be completed within minutes on a standard office computer. By using this approach, multiple repetitions of EMC3-EIRENE simulations that were traditionally required can be simplified into a single simulation. At the same time, it ensures that the simulation results closely align with experimental diagnostic data within the capabilities of EMC3-EIRENE.

The remainder of this paper is organized as follows: section 2 details the experimental diagnostics and the database generation for neural network training. Section 3 presents the neural network architecture and Bayesian inference method. In the section 4, the performance of the proposed method is comprehensively evaluated using experimental data. Finally, section 5 summarizes this work.

2. Experimental diagnostics and dataset generation

W7-X is a five-fold symmetric, quasi-isodynamic stellarator equipped with an island divertor [23, 24]. Its magnetic configurations are established by adjusting the currents in both planar and non-planar toroidal coil sets [25], and are commonly classified by the rotational transform at the plasma edge, $\iota_a = n/m$, where n and m are the toroidal and poloidal mode numbers, respectively.

For this study, an EMC3-EIRENE simulation database has been generated under the standard magnetic configuration ($\iota_a = 5/5$), and the analysis presented here focuses exclusively on experiments performed in this configuration. The edge diagnostics used to optimize the EMC3-EIRENE input parameters include: (1) Divertor spectroscopy [26, 27], which detects CII line emissions (426.8 nm) in the divertor region; (2) Thomson scattering (TS) [28], providing radial electron density and temperature measurements; (3) Divertor Langmuir probes (LPs) [29], which measure ion saturation currents on the horizontal divertors; (4) Divertor thermography [30], capturing heat flux data on divertors. These diagnostics are chosen because they are routinely available on W7-X and, together, cover the plasma state both upstream and downstream in the scrape-off layer (SOL). Figure 1(*a*) illustrates the locations of these diagnostics on W7-X, and figure 1(*b*) shows the horizontal line of sight (LOS) for the divertor spectroscopy at the AEI 51 port, which covers a measurement range of 1 cm–14.5 cm from the horizontal target plate. Since the current EMC3-EIRENE physical model does not account for error fields (which are also not exactly known experimentally) and drift effects, it is unable to reproduce any up-down asymmetry seen in experiments. Therefore, the ion saturation currents from the upper and lower divertor Langmuir probes are averaged for comparisons between experimental and simulated data. A similar approach is taken with the IR camera heat flux measurements, where data from a cross-section near the divertor Langmuir probes are selected.

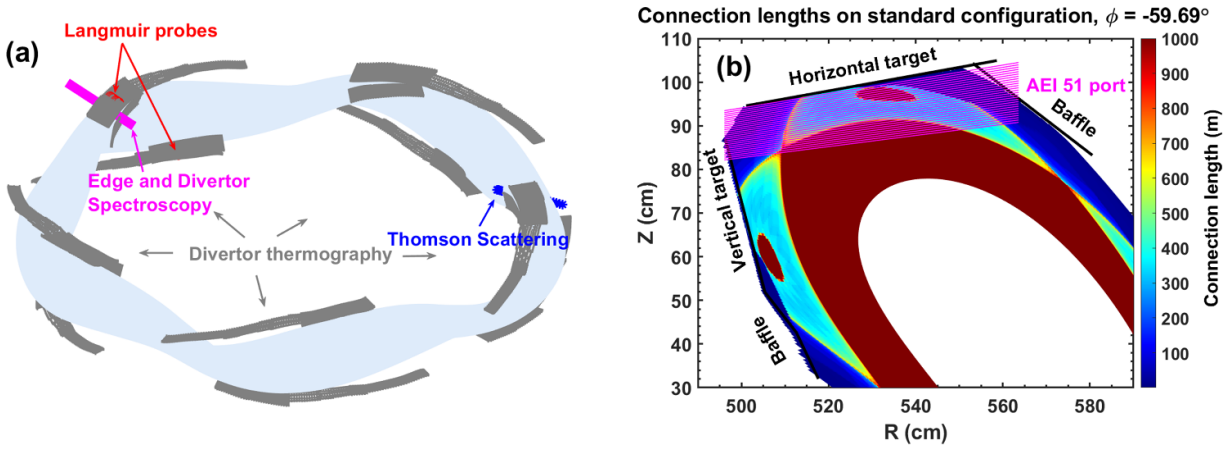

Figure 1. (*a*) The diagram of relevant diagnostic positions in W7-X, and (*b*) the horizontal line of sight (LOS) for the divertor spectroscopy.

To train the neural network model, an EMC3-EIRENE simulation database is created for the standard configuration of W7-X with a heating power of 6 MW. This database consists of four independent parameters, namely the radiation power fraction $f_{\rm rad}$, the separatrix electron density $n_{e,\rm sep}$, and the cross-field particle and thermal diffusivity $D_\perp$ and $\chi_\perp$. It contains 260 simulation cases, each randomly sampled from all possible combinations of four radiation power fraction levels ($f_{\rm rad} = 0.2,\ 0.4,\ 0.6,\ 0.8$), nine separatrix electron densities ($n_{\rm e,sep} = 2.0,\ 3.0,\ 3.5,\ 4.0,\ 4.5,\ 5.0,\ 5.5,\ 6.0,\ 7.0 \times 10^{19}\ \rm m^{-3}$), five cross-field particle diffusivities ($D_\perp = 0.3, 0.5, 0.7, 0.9, 1.1\ \rm m^2\ s^{-1}$), and four thermal diffusivities ($\chi_\perp = 0.6, 0.9, 1.2, 1.5\ \rm m^2\ s^{-1}$). The cross-field particle diffusivities of the main plasma species (hydrogen) and carbon impurities, as well as the cross-field thermal diffusivities of ion and electron, are set equal and assumed to be spatially uniform. In these simulations, carbon sputtered from the divertor and baffle targets is the only radiator, with its source controlled by the total radiated power. After setting the total radiated power $P_{\rm rad}$, EMC3-EIRENE iteratively solves the plasma fluid, impurity transport and neutral equations until the plasma parameters converge. During the iterative process, the impurity transport model incorporates the ADAS database to determine the carbon sputtering flux automatically. For the FNN surrogate model, the input layer comprises these EMC3-EIRENE input parameters, and the output layer represents the synthetic signals generated by each simulation for the above-introduced edge diagnostics. Most of the synthetic quantities can be directly obtained from the standard EMC3-EIRENE outputs, with the exception of the divertor CII signal. The latter is integrated along the LOS of the divertor spectroscopy, using the plasma density and temperature from EMC3-EIRENE and the photon emissivity coefficient (PEC) data from ADAS [31]. The C II signal is calculated from

$$L_{CII} = \sum_i \Delta s_i \sum_j \left(\omega_{ij} \frac{\sum_\sigma \mathrm{PEC}^{(\rm exc)}_{\sigma,k\to l} n_e n_\sigma^{z+} + \sum_\rho \mathrm{PEC}^{(\rm rec)}_{\rho,k\to l} n_e n_\sigma^{(z+1)+} + \sum_\rho \mathrm{PEC}^{(\rm CX)}_{\rho,k\to l} n_H n_\sigma^{(z+1)+}}{4\pi} \right) \tag{1}$$

where $L_{\rm CII}$ denotes the line-emission radiance, the calibrated quantity routinely reported by spectroscopic diagnostics. Δs_i is the length of the ith LOS segment, and ω_{ij} is the ratio of the overlap volume between grid cell j and LOS segment i to the total volume of segment i. $\mathrm{PEC}^{\rm exc}$, $\mathrm{PEC}^{\rm rec}$ and $\mathrm{PEC}^{\rm CX}$ are the photon emissivity coefficients for excitation, recombination and charge exchange, respectively. n_e is the electron density, n_σ^{z+} is the density of the z-times-ionized ion in metastable state σ, n_H is the neutral-hydrogen density, ρ is metastable state, and k, l label the upper and lower atomic levels. The factor ω_{ij} is estimated with a Monte Carlo method. First, N_i random points are distributed inside LOS segment i. The ratio $\frac{N_{ij}}{N_i}$, where N_{ij} is the number of points located inside grid cell j, yields ω_{ij}. This approach avoids geometric intersection calculations. Finally, standardization or normalization is crucial for handling the wide variations in scale and range across different diagnostic data. Without these preprocessing steps, large discrepancies between feature ranges can cause gradient-based optimization methods (e.g. backpropagation [32, 33]) to become skewed toward features with larger numerical values, thereby hindering effective learning and making convergence more difficult. In this work, all synthetic data are scaled by max-value normalization. For each synthetic point we first find its maximum value across the entire data set and then divide every sample by

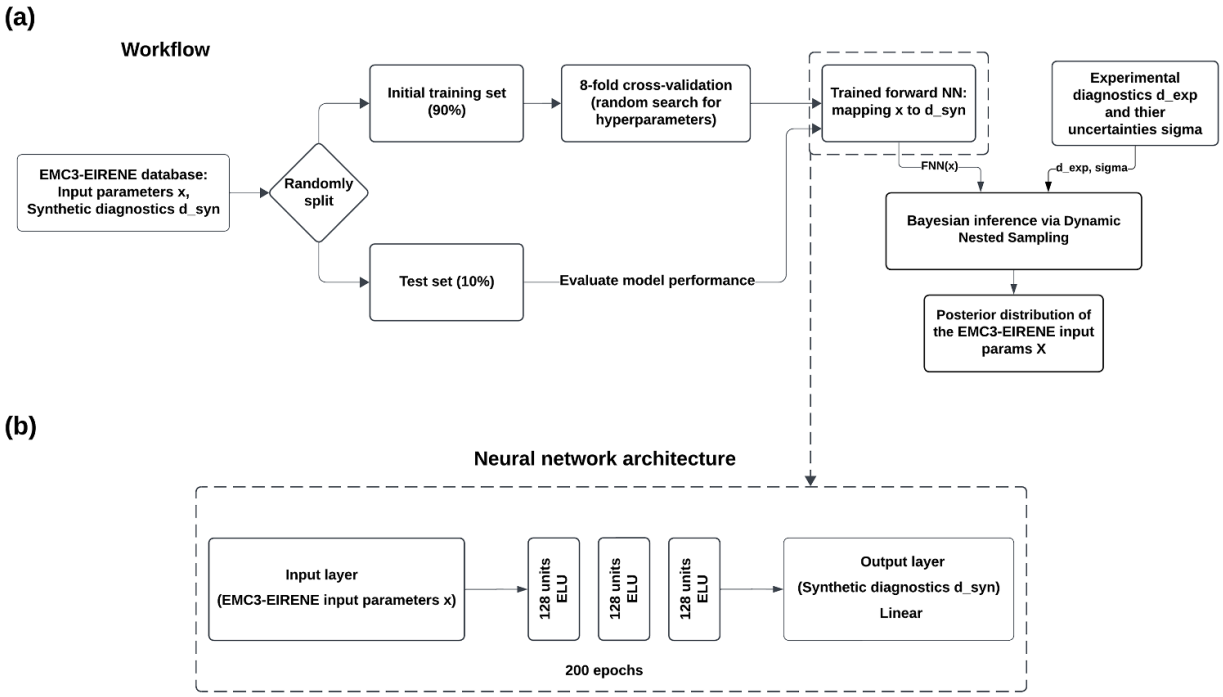

Figure 2. (*a*) Overall workflow of the proposed surrogate-assisted Bayesian inference method, (*b*) schematic representation of the feed-forward neural network architecture.

this value. This places every feature in the [0, 1] range and prevents variables with larger numerical values from dominating the training process.

3. Methods

This section introduces the method for rapidly determining EMC3-EIRENE input parameters that align with experimental data. This method primarily comprises two stages: (1) construction and training of a neural network surrogate model, and (2) Bayesian inference employing Dynamic Nested Sampling. The overall workflow and the neural network architecture are illustrated in figure 2. In brief, the neural network serves as a fast shortcut: for any trial set of EMC3-EIRENE input values it instantly predicts the synthetic data that the full code would produce. The Bayesian framework compares the synthetic data predictions with the experimental measurements and, through the measurement uncertainties, evaluates the likelihood of each trial. This yields a probability-weighted rating of how well every input set reproduces the measurements. Working together, these two steps enable rapid exploration of the input space while still providing reliable, uncertainty-aware estimates of the best-fit parameters. The two stages are discussed in detail in sections 3.1 and 3.2.

3.1. Feed-forward neural network

The feed-forward neural network surrogate model employed here consists of an input layer, multiple hidden layers, and an output layer, with fully connected neurons between adjacent layers. The input layer takes the EMC3-EIRENE input parameters, the hidden layers perform nonlinear transformations to extract higher-level features, and the output layer generates the regression values for the synthetic data. Prior to training, the entire EMC3-EIRENE simulation database—consisting of input parameters paired with corresponding synthetic diagnostic signals—is maximum-normalized and randomly split into an initial training set (90%) and a test set (10%). Hyperparameter optimization is conducted on the initial training set using an 8-fold cross-validation approach. In each fold, the network is trained using seven subsets, while the remaining subset validates model performance. The training loss is quantified by the mean squared error (MSE). Hyperparameter tuning is executed via random search across 200 trials, incorporating L2 regularization to prevent overfitting. Table 1 lists the hyperparameter search ranges along with the optimized values. The final FNN architecture consists of three hidden layers with 128 units per layer, exponential linear units (ELU) activation functions [34], and a linear output layer. Additional optimized hyperparameters are an L2 regularization coefficient of 2.1×10^{-6}, a learning rate of 0.0017, and 200 training epochs with the Adam optimizer [35]. Figure 3 presents the mean training (red) and validation (blue) losses over the eight cross-validation folds obtained with the optimized hyper-parameters. Both curves stabilize after roughly 100 epochs and converge to approximately 0.002, indicating that the network has learned the underlying input-output relationships. After hyperparameter tuning, the model is retrained on the full initial training set using these optimized hyperparameters. Performance evaluation on the independent test set yields an MSE of about 0.002. The neural network is implemented in TensorFlow [36] using the Keras [37] frameworks.

Table 1. Hyperparameter search ranges and optimized settings for neural network training.

Hyperparameters	Search space	Optimized values
Learning rate	0.0001–0.1	**0.0017**
Number of hidden layers	2, 3, 4, 5	**3**
Units per hidden layer	32, 64, 128, 256	**128**
Batch size	8, 16, 32, 64	**16**
L2 regularization coefficient	10^{-6}–10^{-2}	$\mathbf{2.1 \times 10^{-06}}$
Optimizer	Adam	**Adam**
Activation function	ELU, ReLU, Leaky, Tanh	**ELU**
Epochs	50, 100, 200	**200**

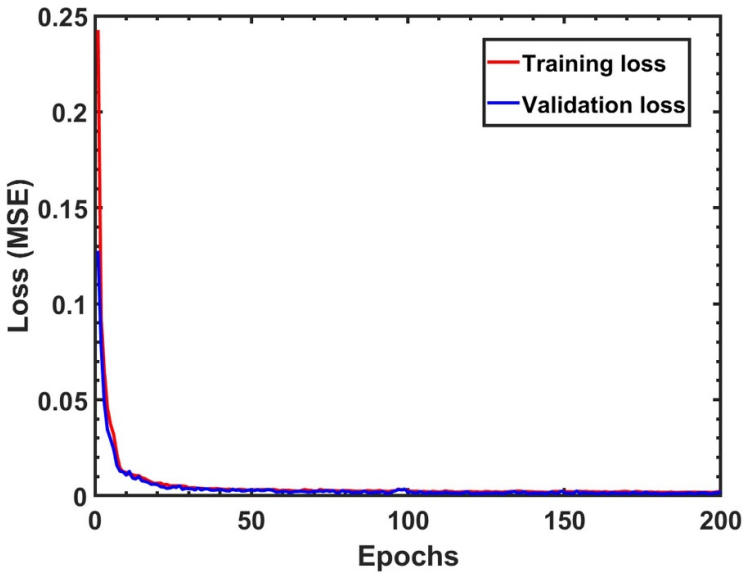

Figure 3. Evolution of average training and validation losses during 8-fold cross-validation with optimized hyperparameters.

A key question is whether the current database is sufficiently large for reliable predictions. To investigate this, the previously optimized hyperparameters and network architecture are kept fixed, while only the trainset fraction (the proportion of data allocated to training) is varied to examine how test loss depends on the training set size. Figure 4 demonstrates test loss versus the fraction of training set, with ten parallel training runs performed at each fraction. As the trainset fraction increases from 0.05 to 0.95, the test loss decreases and then converges. To quantify the convergence point we fitted the mean loss curve with an exponential decay and evaluated how much the loss would still decrease if the trainset were increased by another 5 %. When this additional gain is $< 1\%$ of the current loss value, the improvement is considered negligible. According to this criterion, convergence is reached at a trainset fraction of ≈ 0.55. Beyond about 55% of the full database, adding more samples produces virtually no further reduction in test loss, indicating that the database is already dense enough over the explored input parameter space. Additionally, as the trainset fraction grows, the test losses from the parallel runs exhibit reduced scatter, suggesting greater consistency and stability in the model's performance (i.e. the model becomes less sensitive to the random split).

3.2. Bayesian parameter estimation via Dynamic Nested Sampling

After training the FNN surrogate, we embed it in a Bayesian inference framework employing Dynamic Nested Sampling [22] to infer the EMC3-EIRENE input parameters that best reproduce the experimental data. Bayesian inference can provide the posterior probability distribution of EMC3-EIRENE input parameters (θ) given the experimental measurements (D) and the FNN surrogate model (M). Bayes' theorem gives

$$P(\theta|D,M) = \frac{P(D|\theta,M)\,P(\theta|M)}{P(D|M)} \tag{2}$$

where $P(\theta|D,M)$ represents the posterior distribution of the input parameters θ given the experimental measurements D and the FNN model M. $P(D|\theta,M)$ is the likelihood function that quantifies the agreement between the FNN-predicted synthetic data and the experimental measurements for a given set of input parameters θ. $P(\theta|M)$ is the prior distribution, representing initial belief about input parameters θ before observing the experimental measurements D. $P(D|M)$ is the evidence (or marginal likelihood), calculated by integrating

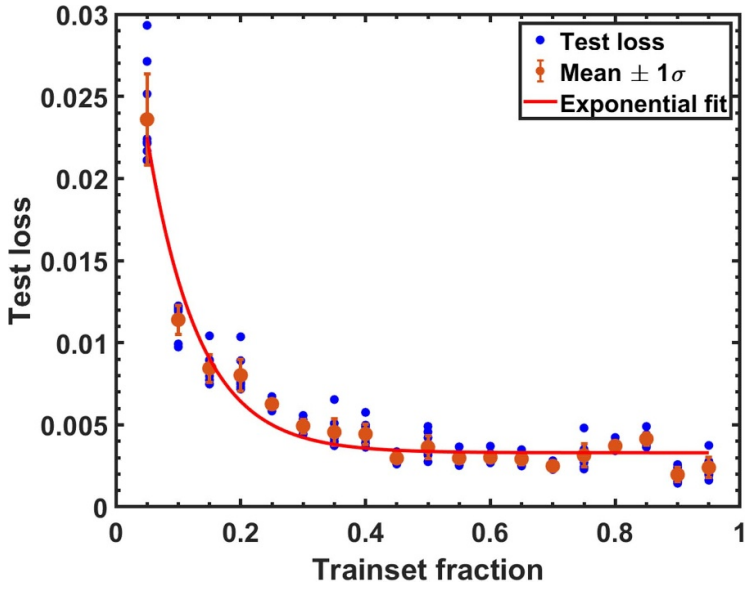

Figure 4. Test loss versus the fraction of the dataset used for training.

over the input parameters θ:

$$P(D|M) = \int P(D|\theta, M)P(\theta|M)\mathrm{d}\theta. \quad (3)$$

A broader parameter space is adopted than that originally covered by the EMC3-EIRENE database, specifically $f_{\mathrm{rad}} = 0.1 - 0.9$, $n_{\mathrm{e,sep}} = 1 - 8 \times 10^{19}$ m^{-3}, $D_{\perp} = 0.1 - 1.3$ m^2 s^{-1}, $\chi_{\perp} = 0.3 - 1.8$ m^2 s^1. Truncated Gaussian priors are used for f_{rad} and $n_{e,\mathrm{sep}}$ because experimental observations constrain their feasible ranges, while uniform priors are chosen for the cross-field particle diffusivity $D_{\perp}$ and thermal diffusivity $\chi_{\perp}$. Synthetic data predicted by the FNN for input parameters that fall marginally outside the original database still closely match new EMC3-EIRENE simulations, confirming that the modest enlargement of the search domain is justified (see figure 7). In the likelihood function, experimental measurement errors are assumed to be Gaussian. In addition to the four diagnostics mentioned above, the bolometer-derived radiated fraction $f_{\mathrm{rad,exp}}$ is incorporated to better constrain EMC3-EIRENE input parameter f_{rad}. Without this constraint, f_{rad} may sometimes deviate significantly from the experimental measurement $f_{\mathrm{rad,exp}}$. Dynamic Nested Sampling (implemented in the dynesty package [38, 39]) adaptively allocates samples based on the likelihood and prior, computes the evidence, and produces accurate posterior distributions. Compared to standard Nested Sampling [40, 41], Dynamic Nested Sampling allocates samples more efficiently, enhancing both parameter estimation and evidence calculation accuracy. In our workflow, dynesty performs the Bayesian inference and a feed-forward neural-network surrogate of EMC3-EIRENE replaces the costly forward model. From the diagnostic measurements and their uncertainties, this method infers the most probable input parameters (f_{rad}, $n_{e,\mathrm{sep}}$, $D_{\perp}$ and $\chi_{\perp}$) used for conventional EMC3-EIRENE code. Using these inferred inputs, a single full EMC3-EIRENE run produces 3D edge-plasma simulation consistent with the diagnostic measurements.

4. Performance evaluation of the proposed method using experimental data

In this section, the applicability of the proposed surrogate-assisted Bayesian method is evaluated by comparing EMC3-EIRENE simulation results with experimental measurements from a density ramp-up discharge (#20181010.028) with the standard magnetic configuration. This discharge covers different divertor operational regimes for assessing the performance of the method. Figure 5 shows the temporal evolution of main plasma parameters during this discharge. As the line-integrated electron density rises, the bolometer-detected radiation power increases correspondingly. While the line-integrated electron density reaches and remains at the detachment threshold ($\sim 11.7 \times 10^{19}$m^{-2}), the radiation power gradually increases, eventually establishing a stable detachment. After 6.5 s, once divertor nozzle hydrogen fueling is turned off, the plasma density begins to decrease, causing the radiation level to progressively decline. We selected three different time points ($t1$, $t2$, and $t3$) with the corresponding radiation fractions ($f_{\mathrm{rad}} = \frac{P_{\mathrm{rad}}}{P_{\mathrm{ECRH}}}$) of 20%, 50%, and 80%, to assess the performance of the proposed method in different plasma scenarios.

Before performing Bayesian inference, it is crucial to quantify the uncertainties for each experimental diagnostic. Figures 7–9 present detailed diagnostic profiles at each selected radiation fraction. As the Thomson scattering system on W7-X was not optimized for boundary measurements, its edge error bars are relatively large. In this discharge, Thomson scattering is performed at a temporal resolution of 30 Hz, and measurements from five consecutive time points around each selected moment are averaged. The overall uncertainties for Thomson scattering (σ_{TS}) are estimated by combining the measurement uncertainties and temporal variability as follows $\sigma_{\mathrm{TS}} = \sqrt{\sigma^2_{\mathrm{measurement}} + \sigma^2_{\mathrm{time}}}$, where $\sigma_{\mathrm{measurement}}$ is the average uncertainty of the five individual measurements,

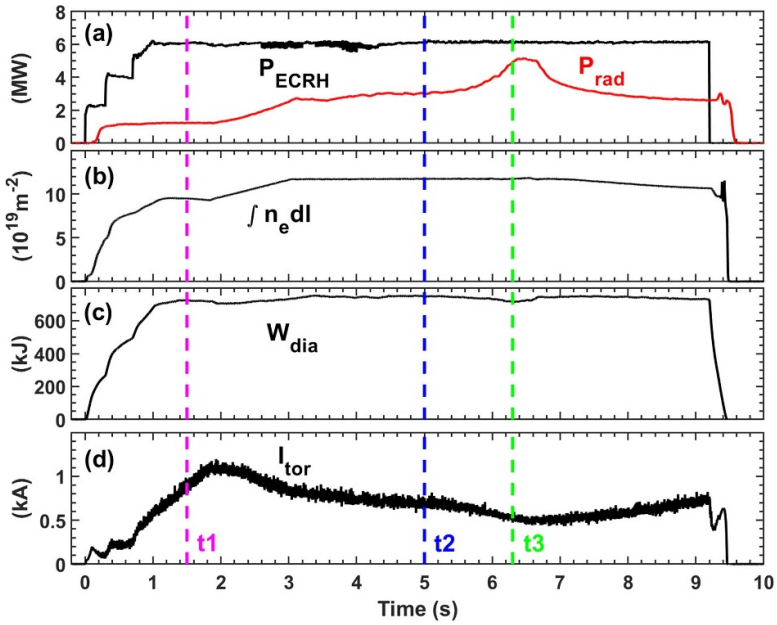

Figure 5. Time evolution of a density ramp-up detachment discharge (#20181010.028) on W7-X, including (*a*) ECRH heating power and total radiated power, (*b*) line-integrated electron density, (*c*) diamagnetic energy, and (*d*) toroidal plasma current. Dashed vertical lines indicate three specific times selected for parameter estimation.

and σ_{time} is the standard deviation of these measurements. For ion saturation current and heat flux on targets, significant asymmetries exist between measurements at different divertor locations, greatly exceeding instrumental uncertainty. Thus, the uncertainty for these diagnostics is estimated using the standard deviation of the asymmetric values. For the divertor CII radiance measurements, the uncertainty has not been precisely quantified. Therefore, based on empirical experience, we assume an uncertainty of 30% (i.e. $\sigma_{\text{CII}} = 30\% \times I_{\text{CII}}$). Similarly, the bolometer-derived radiation fraction uncertainty is set at 20%.

Figure 6 shows corner plots of the posterior distributions for EMC3-EIRENE input parameters (f_{rad}, $n_{e,\text{sep}}$, $D_\perp$ and $\chi_\perp$) obtained using the proposed method under the three selected radiation fraction conditions. Diagonal plots display probability distribution histograms, with the central dashed lines indicating median parameter values and side dashed lines marking one-standard-deviation (σ) uncertainty intervals. The specific median values and corresponding uncertainties ($+\sigma$ and $-\sigma$) for each parameter are explicitly indicated above each histogram. Below the diagonal, joint distributions between parameter pairs are illustrated. Contours close to circular indicate weak correlations between corresponding parameters, whereas elliptical contours with distinctly inclined major axes suggest stronger linear correlations.

To further validate these predictions, EMC3-EIRENE simulations were conducted using the input parameters corresponding to the maximum *a posteriori* (MAP) estimate, which is the parameter set with the highest posterior likelihood, and the simulation results were then compared with the experimental data. For radiation fractions of approximately 20%, 50%, and 80%, the MAP estimates were determined to be $f_{\text{rad}} = 0.23,\ 0.60,$ and 0.79; $n_{\text{e,sep}} = 2.92,\ 5.00,$ and $4.87\ \times 10^{19}\text{m}^{-3}$; $D_\perp = 1.34,\ 1.09,$ and $0.82\ \text{m}^2\ \text{s}^{-1}$; $\chi_\perp = 1.37,\ 0.82,$ and $1.34\ \text{m}^2\ \text{s}^{-1}$. Figure 7 compares EMC3-EIRENE simulations, FNN surrogate predictions, and experimental data for the 20% radiation fraction scenario, showing profiles of electron density n_e, electron temperature T_e, horizontal divertor heat flux at a toroidal angle of $-82°$, divertor ion saturation current j_{sat} from divertor Langmuir probes, and divertor CII radiance measured by the AEI 51 spectroscopy system. In each plot, black dots or solid lines represent experimental measurements, blue crosses are the FNN surrogate predictions at the MAP input set returned by the Bayesian inference (shown only as an intermediate check), and red lines correspond to EMC3-EIRENE simulation results obtained using the MAP estimates. The FNN predictions and the EMC3-EIRENE simulations agree well, demonstrating the FNN surrogate model's good performance in capturing the relationship between the EMC3-EIRENE input parameters and synthetic diagnostic data. Additionally, the EMC3-EIRENE results match the experimental measurements satisfactorily for n_e, T_e, j_{sat}, and CII radiance, although the simulated heat flux has a broader profile than the observed data.

For the scenario with a 50% radiation fraction, figure 8 shows that both the target heat flux and ion saturation current decrease slightly, accompanied by a reduction in asymmetry. The surrogate model maintains strong agreement with EMC3-EIRENE simulations, further validating its applicability at intermediate radiation levels. Comparison of EMC3-EIRENE simulations with experimental data shows good agreement for TS n_e, T_e, divertor heat flux, and divertor ion saturation, but a discrepancy is observed in the spatial location of the CII radiance peak. At an 80% radiation fraction, divertor heat flux and ion saturation current decrease significantly, and impurity ion penetration increases, shifting the CII radiance further

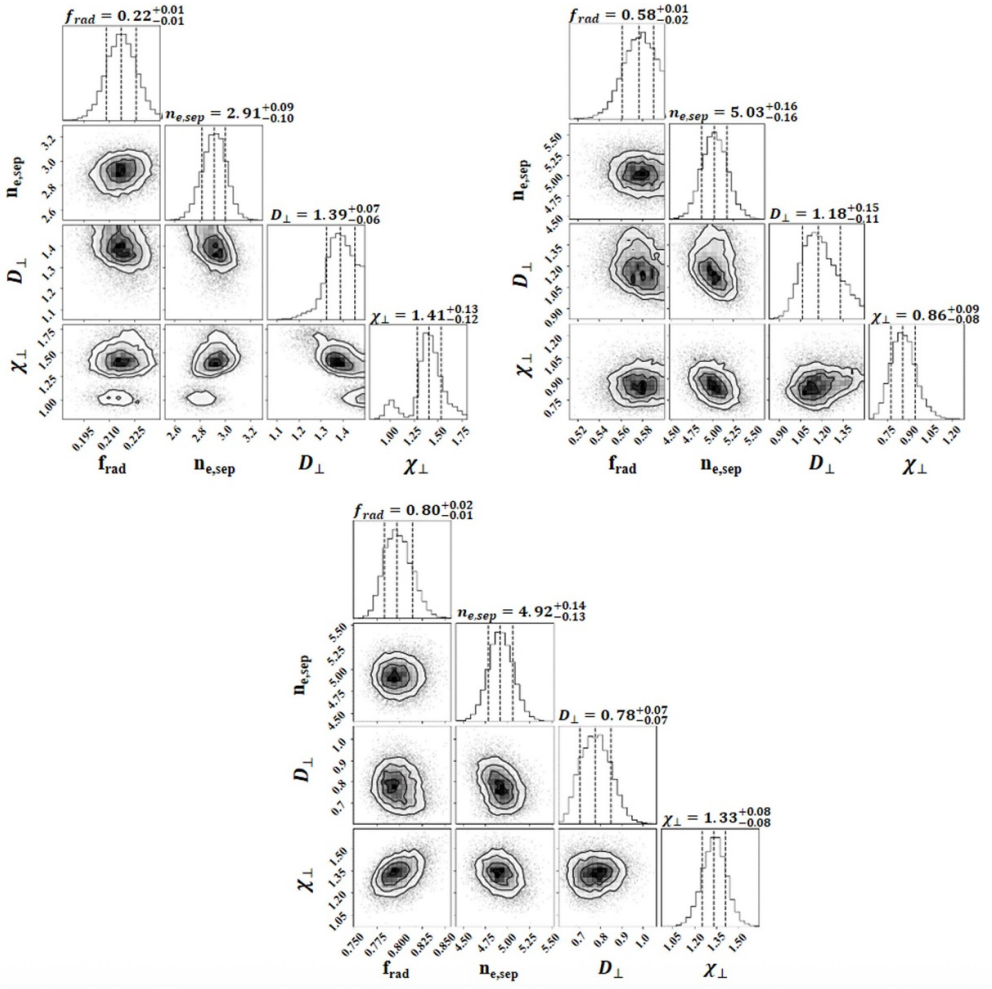

Figure 6. Corner plots of posterior distributions of EMC3-EIRENE input parameters at different radiation fractions.

away from the target. Figure 9 shows a slight increase in the difference between the EMC3-EIRENE simulations and FNN predictions, which may be attributed to relaxed convergence criteria for higher radiation fraction cases in the training database (where a relative change of less than 1% is considered converged, compared to less than 0.7% for lower f_{rad} cases). Similar to the 50% f_{rad} scenario, the spatial mismatch between simulated and experimental CII radiance peaks persists, aligning with observations reported in previous studies [26]. One possible explanation for this discrepancy is the assumption of uniform cross-field transport coefficients in EMC3-EIRENE. In reality, spatial variations in these coefficients can modify the balance between parallel and perpendicular transport, thereby influencing impurity distributions [42, 43]. Another potential factor might be the absence of drift effects in EMC3-EIRENE. Significant radiation asymmetry is observed in experiments [9, 44], but the lack of drift effects in EMC3-EIRENE may prevent the simulation from reproducing the CII radiance. Overall, within the capabilities of EMC3-EIRENE, the proposed method achieves satisfactory agreement between simulated and measured diagnostics across different radiation fractions. Nevertheless, comprehensive validation of synthetic divertor spectroscopy predictions requires further investigations.

5. Summary

In this study, a 260-case EMC3-EIRENE simulation database was generated by scanning four key input parameters—namely the radiation power fraction f_{rad}, separatrix electron density $n_{e,\mathrm{sep}}$, and cross-field particle diffusivity $D_\perp$ and thermal diffusivity $\chi_\perp$. A feed-forward neural network was then trained to map the EMC3-EIRENE input parameters to synthetic diagnostic data, using 8-fold cross-validation and random search for hyperparameter optimization. Compared to full EMC3-EIRENE simulations, the trained FNN surrogate model can quickly predict synthetic diagnostic data from a given input parameter set.

The trained FNN surrogate model was embedded in a Bayesian inference framework using Dynamic Nested Sampling to estimate the posterior distributions of EMC3-EIRENE input parameters by incorporating experimental diagnostic measurements along with their associated

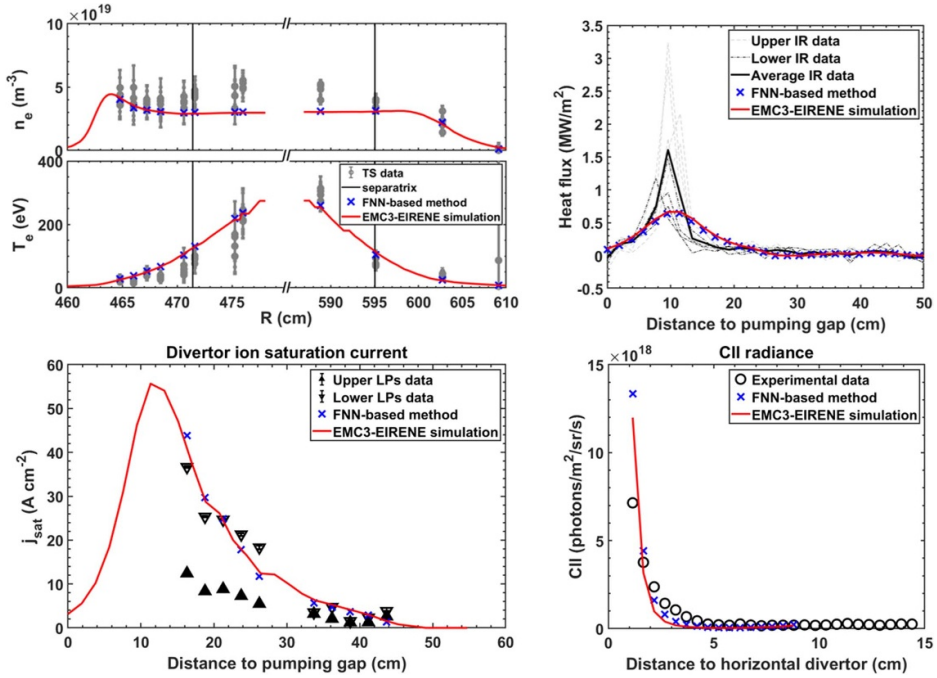

Figure 7. Comparison between experimental data, FNN surrogate predictions, and EMC3-EIRENE simulations using MAP input parameters at 20% radiation fraction.

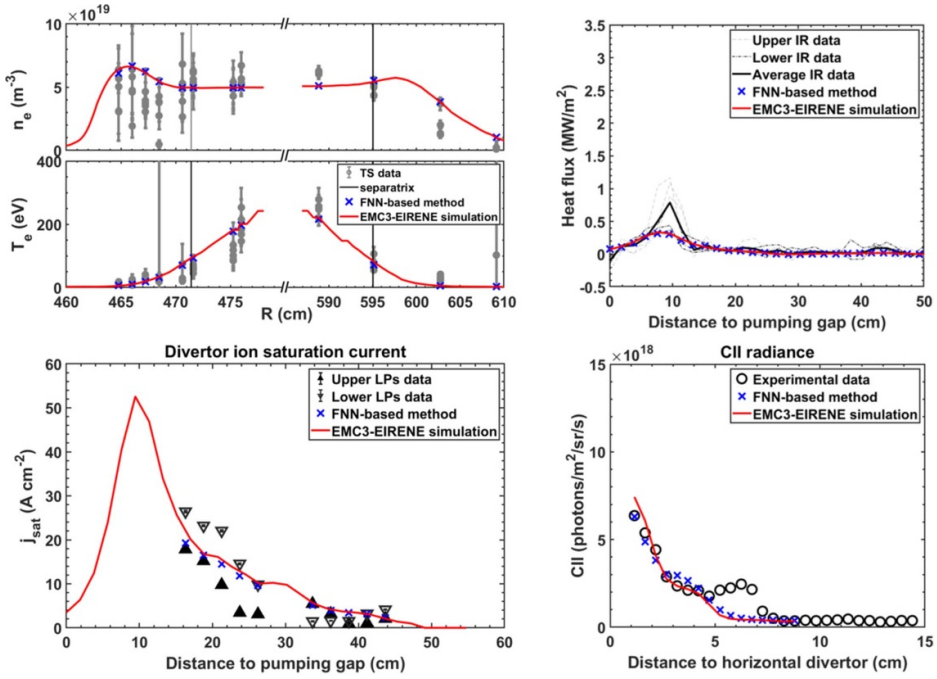

Figure 8. Comparison between experimental data, FNN surrogate predictions, and EMC3-EIRENE simulations at 50% radiation fraction.

uncertainties. Because the surrogate generates synthetic data almost instantaneously, the inference is greatly accelerated and a comprehensive exploration of parameter space is achieved. Full EMC3-EIRENE simulations conducted with MAP estimates of input parameters at different radiation fraction levels showed satisfactory agreement with experimental observations, highlighting the effectiveness of the proposed method.

In summary, the neural-network surrogate gives rapid predictions across the input-parameter space, and the Bayesian framework compares those predictions with the experimental data while fully accounting for the measurement uncertainties. Together, these two tools make it possible to find the EMC3-EIRENE inputs that best match the observations, especially the otherwise unknown free parameters cross-field transport coefficients. The main highlights of our work focus on

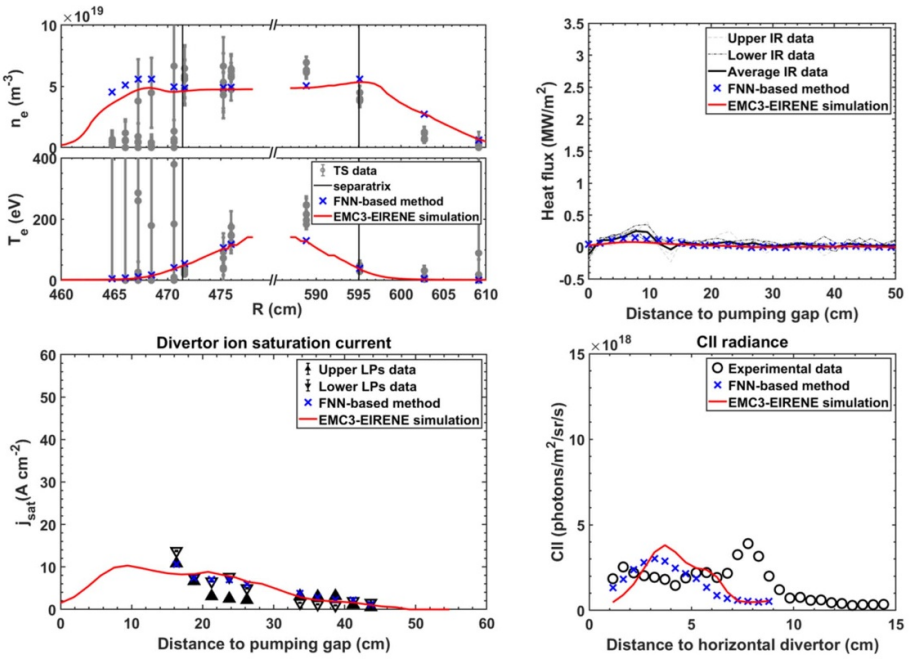

Figure 9. Comparison between experimental data, FNN surrogate predictions, and EMC3-EIRENE simulations at 80% radiation fraction.

the post-experimental physical analysis, which can be summarized in the following three points: (1) A Bayesian neural network fast infer the cross-field transport coefficients that characterize the edge plasma transport properties, thereby helping to understand the transport behavior under different plasma conditions; (2) The Bayesian neural network performs an uncertainty-aware inversion that yields posterior estimates for f_{rad} and $n_{e,\mathrm{sep}}$, updating their uncertainties using all selected diagnostics. (3) By feeding the Bayesian-inferred inputs (f_{rad}, $n_{\mathrm{e,sep}}$, $D_{\perp}$ and $\chi_{\perp}$) into EMC3-EIRENE, a single run reproduces the 3D edge plasma distributions consistent with the experimental observations, eliminating the need for extensive parameter scans. This work is focused on developing and validating the method's feasibility. The current EMC3-EIRENE database is still being expanded and therefore does not yet cover the full W7-X operating space, for example the complete range of heating powers, and different magnetic configurations. Future work will expand the database and extend the range of synthetic data, thereby broadening the applicability of the neural network-based method.

Acknowledgment

The project this report was supported with funds from the German Federal Ministry of Education and Research in the Förderprogramm 'Fusion 2040– Forschung auf dem Weg zum Fusionskraftwerk', Contract Number 13F1012C. The sole responsibility for the report's contents lies with the authors. This work has also been carried out within the framework of the EUROfusion Consortium, funded by the European Union via the Euratom Research and Training Programme (Grant Agreement No. 101052200—EUROfusion). Views and opinions expressed are however those of the author(s) only and do not necessarily reflect those of the European Union or the European Commission. Neither the European Union nor the European Commission can be held responsible for them.

The authors gratefully acknowledge the computing time granted by the JARA-HPC Vergabegremium and VSR commission on the supercomputer JURECA at Forschungszentrum Jülich.

ORCID iDs

Y. Luo 0000-0003-2319-1172
S. Xu 0000-0002-0033-3468
Y. Liang 0000-0002-9483-6911
E. Wang 0000-0001-7828-1162
Y. Feng 0000-0002-3846-4279
A. Knieps 0000-0003-0083-7188
S. Brezinsek 0000-0002-7213-3326
D. Zhang 0000-0002-5800-4907
Y. Gao 0000-0001-8576-0970
M. Jakubowski 0000-0002-6557-3497

References

[1] Feng Y., Sardei F., Kisslinger J. and Grigull P. 1997 *J. Nucl. Mater.* **241** 930
[2] Feng Y., Sardei F. and Kisslinger J. 1999 *J. Nucl. Mater.* **266** 812
[3] Reiter D., Baelmans M. and Börner P. 2005 *Fusion Sci. Technol.* **47** 172
[4] Effenberg F. *et al* 2017 *Nucl. Fusion* **57** 036021
[5] Xu S. *et al* 2018 *Nucl. Fusion* **58** 106008
[6] Xu S. *et al* 2020 *Nucl. Fusion* **60** 056006
[7] Feng Y. *et al* 2021 *Nucl. Fusion* **61** 086012
[8] Xu S. *et al* 2023 *Nucl. Fusion* **63** 066005

[9] Winters V.R. *et al* 2024 *Nucl. Fusion* **64** 056042
[10] Feng Y. *et al* 2024 *Nucl. Fusion* **64** 086027
[11] Feng Y. *et al* 2021 *Nucl. Fusion* **61** 106018
[12] Winters V. *et al* 2024 *Nucl. Fusion* **64** 126047
[13] Seo J., Na Y.S., Kim B., Lee C.Y., Park M.S., Park S.J. and Lee Y.H. 2021 *Nucl. Fusion* **61** 106010
[14] Degrave J. *et al* 2022 *Nature* **602** 414
[15] Seo J., Kim S., Jalalvand A., Conlin R., Rothstein A., Abbate J., Erickson K., Wai J., Shousha R. and Kolemen E. 2024 *Nature* **626** 746
[16] Kates-Harbeck J., Svyatkovskiy A. and Tang W. 2019 *Nature* **568** 526
[17] Fu Y.C. *et al* 2020 *Phys. Plasmas* **27** 022501
[18] Cai J.Q. *et al* 2024 *Plasma Sci. Technol.* **26** 055102
[19] Meneghini O. *et al* 2017 *Nucl. Fusion* **57** 036021
[20] van de Plassche K.L., Citrin J., Bourdelle C., Camenen Y., Casson F.J., Dagnelie V.I., Felici F., Ho A. and Van Mulders S. 2020 *Phys. Plasmas* **27** 022310
[21] Dasbach S. and Wiesen S. 2023 *Nucl. Mater. Energy* **34** 101396
[22] Higson E., Handley W., Hobson M. and Lasenby A. 2019 *Stat. Comput.* **29** 891
[23] Renner H., Boscary J., Greuner H., Grote H., Hoffmann F.W., Kisslinger J., Strumberger E. and Mendelevitch B. 2002 *Plasma Phys. Control. Fusion* **44** 1005
[24] König R. *et al* 2002 *Plasma Phys. Control. Fusion* **44** 2365
[25] Geiger J., Beidler C.D., Feng Y., Maassberg H., Marushchenko N.B. and Turkin Y. 2015 *Plasma Phys. Control. Fusion* **57** 014004
[26] Krychowiak M. 2021 *47th EPS Conf. on Plasma Physics* (*online*, *21–25 June 2021*) (available at: https://epsplasma2020.eu/)
[27] Liang Y. *et al* 2017 *Nucl. Fusion* **57** 066049
[28] Pasch E., Beurskens M.N.A., Bozhenkov S.A., Fuchert G., Knauer J. and Wolf R.C. (W7-X Team) 2016 *Rev. Sci. Instrum.* **87** 11E729
[29] Laube R., Laux M., Ye M.Y., Greuner H. and Lindig S. 2011 *Fusion Eng. Des.* **86** 1133
[30] Jakubowski M. *et al* 2018 *Rev. Sci. Instrum.* **89** 10E116
[31] Summers H.P. and O'Mullane M.G. 2011 *AIP Conf. Proc.* **1344** 179
[32] Leung H. and Haykin S. 1991 *IEEE Trans. Signal Process.* **39** 2101
[33] Benvenuto N. and Piazza F. 1992 *IEEE Trans. Signal Process.* **40** 967
[34] Clevert D.-A., Unterthiner T. and Hochreiter S. 2015 arXiv:1511.07289
[35] Kingma D.P. 2014 arXiv:1412.6980
[36] Abadi M. *et al* 2016 arXiv:1603.04467
[37] Keras 2015 Keras: Deep Learning for humans (available at: https://keras.io)
[38] Speagle J.S. 2020 *Mon. Not. R. Astron. Soc.* **493** 3132
[39] Koposov S. *et al* 2024 Zenodo joshspeagle/dynesty: v2.1.4 (available at: https://zenodo.org/records/12537467)
[40] Skilling J. 2004 *Bayesian Inference and Maximum Entropy Methods in Science and Engineering* vol 735 (Springer) p 395
[41] Skilling J. 2006 *Bayesian Anal.* **1** 833
[42] Luo Y. *et al* 2023 *49th EPS Conf. on Plasma Physics* (*Bordeaux, France*, *03–07 July 2021*)
[43] Bold D., Reimold F., Niemann H., Gao Y., Jakubowski M., Killer C., Winters V.R. and Maaziz N. (W7-X Team) 2024 *Nucl. Fusion* **64** 126055
[44] Zhang D. *et al* 2021 *Nucl. Fusion* **61** 116043